Evaluation of Spatial Errors of Precipitation Rates and Types from TRMM Spaceborne Radar over the Southern CONUS

S. CHEN,* P. E. KIRSTETTER,+ Y. HONG,* J. J. GOURLEY,# Y. D. TIAN,@ Y. C. QI,& Q. CAO,* J. ZHANG,# K. HOWARD,# J. J. HU,** AND X. W. XUE*

* *School of Civil Engineering and Environmental Science, University of Oklahoma, and Advanced Radar Research Center, National Weather Center, Norman, Oklahoma*

\+ *School of Civil Engineering and Environmental Science, University of Oklahoma, and Advanced Radar Research Center, National Weather Center, and NOAA/National Severe Storms Laboratory, Norman, Oklahoma*

\# *NOAA/National Severe Storms Laboratory, Norman, Oklahoma*

@ *Earth System Science Interdisciplinary Center, University of Maryland, College Park, College Park, and Hydrological Sciences Laboratory, NASA Goddard Space Flight Center, Greenbelt, Maryland*

& *NOAA/National Severe Storms Laboratory, and Cooperative Institute for Mesoscale Meteorological Studies, University of Oklahoma, Norman, Oklahoma*

** *School of Computer Science, University of Oklahoma, Norman, Oklahoma*

(Manuscript received 11 February 2013, in final form 13 June 2013)

ABSTRACT

In this paper, the authors estimate the uncertainty of the rainfall products from NASA and Japan Aerospace Exploration Agency's (JAXA) Tropical Rainfall Measurement Mission (TRMM) Precipitation Radar (PR) so that they may be used in a quantitative manner for applications like hydrologic modeling or merging with other rainfall products. The spatial error structure of TRMM PR surface rain rates and types was systematically studied by comparing them with NOAA/National Severe Storms Laboratory's (NSSL) next generation, high-resolution (1 km/5 min) National Mosaic and Multi-Sensor Quantitative Precipitation Estimation (QPE; NMQ/Q2) over the TRMM-covered continental United States (CONUS). Data pairs are first matched at the PR footprint scale (5 km/instantaneous) and then grouped into 0.25° grid cells to yield spatially distributed error maps and statistics using data from December 2009 through November 2010. Careful quality control steps (including bias correction with rain gauges and quality filtering) are applied to the ground radar measurements prior to considering them as reference data. The results show that PR captures well the spatial pattern of total rainfall amounts with a high correlation coefficient (CC; 0.91) with Q2, but this decreases to 0.56 for instantaneous rain rates. In terms of precipitation types, Q2 and PR convective echoes are spatially correlated with a CC of 0.63. Despite this correlation, PR's total annual precipitation from convection is 48.82% less than that by Q2, which points to potential issues in the PR algorithm's attenuation correction, nonuniform beam filling, and/or reflectivity-to-rainfall relation. Finally, the spatial analysis identifies regime-dependent errors, in particular in the mountainous west. It is likely that the surface reference technique is triggered over complex terrain, resulting in high-amplitude biases.

1. Introduction

Reliable quantitative estimates of the spatial precipitation distribution are critical in the application of satellite-based rainfall in hydrologic modeling and hazards monitoring and forecasting. Because of their global coverage and spatial continuity, satellite-based quantitative precipitation estimates (QPE) products are used for such applications. However, there are many inherent error sources in satellite-based measurements, such as the spatial horizontal/vertical heterogeneity of the rain fields. Therefore, characterizing the error structure of satellite-based rainfall products is recognized as a major issue for the usefulness of the estimates (Abdella and Alfredsen 2010; Wolff and Fisher 2009; Yang et al. 2006; Zeweldi and Gebremichael 2009). In addition, a quantification of the error characteristics is necessary for data assimilation, climate analysis (Li et al. 2012; Stephens and Kummerow 2007), and hydrological modeling of

Corresponding author address: Dr. Yang Hong, National Weather Center, Advanced Radar Research Center, Suite 4610, 120 David L. Boren Blvd., Norman, OK 73072-7303.
E-mail: yanghong@ou.edu

DOI: 10.1175/JHM-D-13-027.1

© 2013 American Meteorological Society

natural hazards (Grimes and Diop 2003; Hong and Adler 2007; Lebel et al. 2009; Li et al. 2012; Parkes et al. 2013).

The first space-based precipitation radar (PR) was launched aboard the Tropical Rainfall Measuring Mission (TRMM) in 1997. TRMM is a joint mission between the National Aeronautics and Space Administration (NASA) and the Japan Aerospace Exploration Agency (JAXA) designed to monitor and study tropical rainfall. In addition to PR, other precipitation-related instruments include the TRMM Microwave Imager (TMI), the Visible Infrared Scanner (VIRS), and the Lightning Imaging Sensor (LIS; Kummerow et al. 1998). PR measures the rainfall conjointly with TMI; it measures the 3D rainfall distribution over both land and ocean, whereas TMI, as well as many other passive microwave sensors aboard other satellite platforms, provides an indirect measurement of surface rainfall. Therefore, TRMM PR rainfall estimates are considered as a reference for calibrating TMI-based rainfall estimates (Wolff and Fisher 2009; Yang et al. 2006). The PR-calibrated TMI, in turn, has been used as the reference for other passive microwave sensors, which collectively enable the creation of global-scale precipitation products (Huffman et al. 2007). Thus, PR has fundamental impacts on satellite-based rainfall estimates from other low-Earth-orbiting passive microwave measurements and a number of satellite-based, high-resolution precipitation products (Berges et al. 2010; Ebert 2007; Hong et al. 2007).

To evaluate the error characteristics of TRMM PR, many studies have been conducted to investigate the quality of PR estimates in different regions in the world (Adeyewa and Nakamura 2003; Amitai et al. 2009; Wolff and Fisher 2009; Wolff et al. 2005). Over the United States, Amitai et al. (2009, 2012) have compared the PR with the National Oceanic and Atmospheric Administration/National Severe Storms Laboratory's (NOAA/NSSL) ground radar-based National Mosaic and Multi-Sensor QPE system (NMQ/Q2) as the U.S. network offers a robust set of resources for validation. However, many of the studies are event based and are limited in terms of breadth of study domain and length of time period. So far, long-term, large-scale studies of PR's performance are rare, largely because of the lack of matching ground references. Following the work described by Kirstetter et al. (2012b), in this paper we carried out studies over the southern continental United States (CONUS) for a long, continuous period, including both warm and cool seasons, with quality-controlled, high-resolution ground radar measurements. Specifically, we performed a comprehensive evaluation for regions over the entire southern CONUS covered by TRMM PR using one year of data from TRMM PR and NOAA/NSSL Q2 data (Zhang et al. 2011) from December 2009 to November 2010. Analyses from this study now reveal the spatial error characteristics of TRMM PR both in terms of rain rates and types. A major outcome of this study is to supply uncertainty estimates for users of the data.

As part of an effort to characterize the error of PR rainfall estimates, this paper builds on a framework developed in Kirstetter et al. (2012b) for comparing space-based measurements to Q2 rainfall. Ongoing efforts are underway to analyze influences of additional error factors on the PR rainfall estimates at ground like nonuniform beam filling (NUBF), rain types, and incidence angle. A complementary interest of the present paper is to map the error so as to provide spatial error information to users of TRMM PR data, including hydrologists, and to identify specific error regimes. These tasks are possible with an accurate rainfall reference at ground. Finally, this study provides a benchmark for the future Global Precipitation Measurement (GPM) Dual-Frequency Precipitation Radar (DPR). The paper is organized as follows. Section 2 describes the ground-based and spaceborne radar data and methods used in this study. Section 3 describes the evaluation results and discussion, including the analysis of spatial error characteristics over TRMM-covered regions of the CONUS. Section 4 provides the summary and conclusion.

2. Data and methods

a. Q2 ground reference data

The ground reference data used in this study are referred to as NMQ/Q2 data. The NMQ system was originally developed from a joint initiative between NSSL, the Salt River Project, and the Federal Aviation Administration/Aviation Weather Research Program. The NMQ system is composed of four major modules: 1) single-radar processing, 2) 3D and 2D radar mosaic, 3) QPE generation (Vasiloff et al. 2007), and 4) evaluation. The data sources include the level 2 (base level) data from the Next Generation Weather Radar (NEXRAD) network, Rapid Update Cycle (RUC) model hourly analyses (Benjamin et al. 2004), and rain gauge observations from the Hydrometeorological Automated Data System network. Two precipitation products from the NMQ system, namely, radar-derived QPE (Q2Rad) at 1-km/5-min resolution and the local gauge-corrected radar product (Q2RadGC) at 1-km/1-h resolution (Zhang et al. 2011) are used in this study. In addition, NMQ provides another important product related to the accuracy of the QPEs called the hybrid scan reflectivity height (HSRH). The HSRH product is available every 5 min and is composed of the lowest effective radar scanning

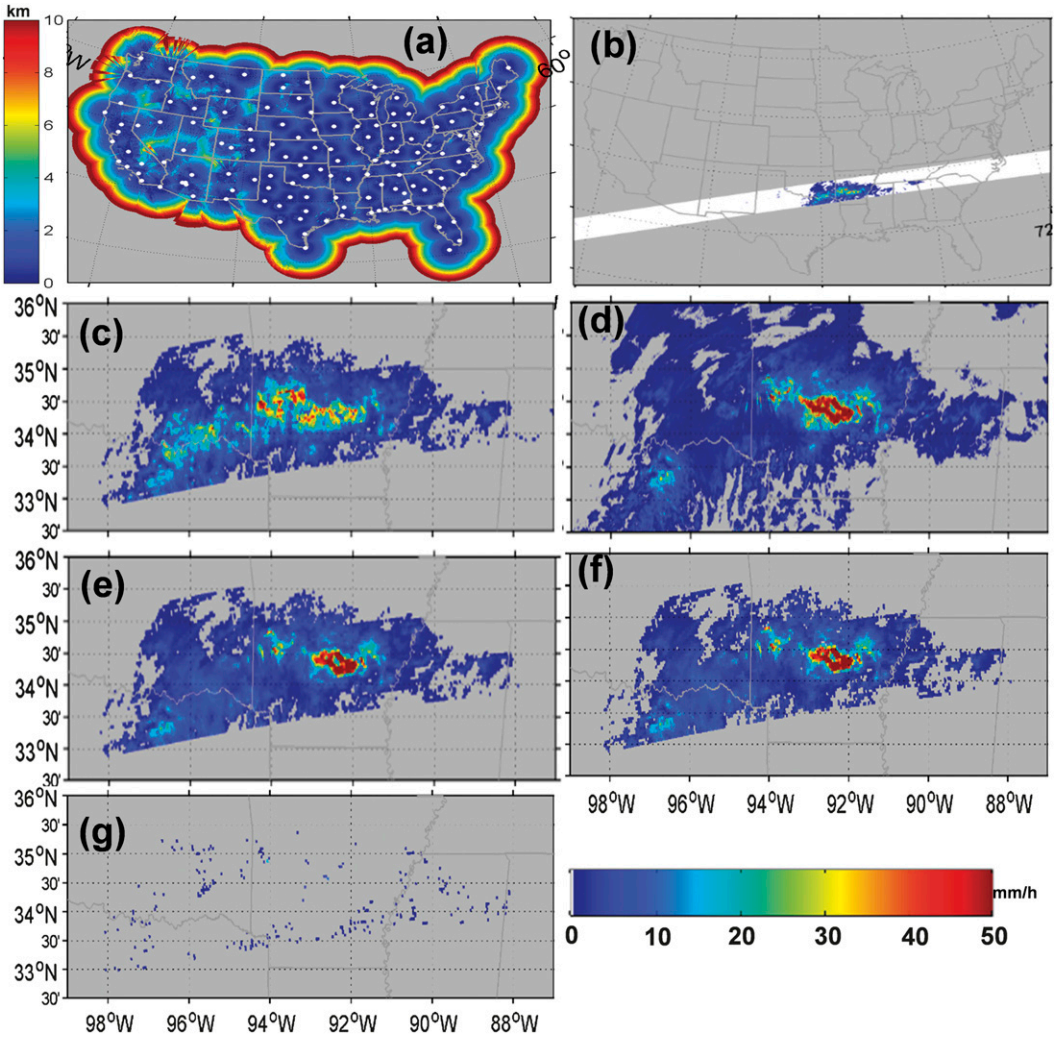

FIG. 1. (a) HSRH and Weather Surveillance Radar-1988 Doppler (WSR-88D) radar locations (shown as white points), (b) overpass of TRMM PR at 1630 UTC 8 Feb 2010, (c) a zoomed-in view of the TRMM 2A25 PR rainfall product of (b),(d) original Q2RadGC rain rate product, (e) Q2RadGC resampled to the TRMM PR pixel resolution, (f) robust Q2RadGC, and (g) nonrobust Q2RadGC.

heights from which the reflectivity data are converted into precipitation according to a certain Z–R relation based on the vertical profile of reflectivity (VPR) classification (Zhang et al. 2011). Figure 1a shows the HSRH product over the CONUS. Relatively high HSRH values are present in the Intermountain West because of intervening beam blockages (Maddox et al. 2002). Finally, we used the precipitation-type product from Q2 to infer potential error characteristics due to precipitation classification. Both Q2 and PR algorithms base their surface rainfall rate estimates on the classification of the precipitation type (e.g., convective versus stratiform) for a given grid column. Thus, there may be errors that are merely due to improper classification. Q2 identifies convective echoes if there is reflectivity >50 dBZ anywhere in the grid column or reflectivity >30 dBZ at temperatures colder than the −10°C isotherm. Otherwise, it is considered as stratiform in our study.

To obtain an instantaneous, low-bias rain rate mosaic, we applied a bias-correction method similar to the one proposed by Amitai et al. (2012) to yield the Q2RadGC product at 5-min resolution. We compared the hourly Q2Rad and Q2RadGC products to compute the bias on a pixel-by-pixel basis. The hourly correction factor was then applied to the Q2Rad product every 5 min. While the true, unknown rainfall bias may vary at a given pixel within an hour, the adjustment scheme we applied at least provides for the removal of hourly bias applied downscale to rainfall rates. Extreme adjustment factors (outside 0.1–10) were discarded and no comparison is

performed with PR for the corresponding Q2 values (Kirstetter et al. 2012b). Additional details regarding the processing of the Q2 reference are provided in section 2c with a discussion on the PR-Q2 matching methodology.

b. TRMM PR

The TRMM PR is the first precipitation radar operating in space. It operates at 13.8 GHz and measures the 3D rainfall distribution over both land and ocean, and it defines the layer depth of the precipitation. It covers the tropics from 37°S to 37°N, with a spatial horizontal resolution of 4.3 km before the orbit boost on 7 August 2001, which increased to 5.0 km after the boost, and a vertical resolution of 250 m. Its radar wavelength is 2.2 cm and the minimum detectable echo is about 17 dBZ, which is equivalent to about 0.5 mm h^{-1} (Kozu et al. 2001; Kummerow et al. 1998). A study by Kirstetter et al. (2012a) show that version 7 of the PR underestimates light rain rates (<0.3 mm h^{-1}) and high rain rates (>10 mm h^{-1}). The TRMM PR product used in this study is the version 7, level 2 product 2A25. Figure 1b shows an example of a TRMM PR pass over the southern CONUS at 1630 UTC 8 February 2010.

c. Data matching and evaluation

The time and space resolution of the reference rainfall should be carefully matched to the TRMM PR pixel resolution as closely as possible in order to quantitatively evaluate PR. Otherwise, systematic and random errors may arise because of data mismatches rather than reflecting the accuracy of the product. The Q2 products closest in time to the TRMM satellite local overpass schedule time are used and resampled to the PR spatial resolution. TRMM essentially provides a snapshot at a given time while Q2-based rainfall estimates are produced every 5 min. This equates to a maximum temporal offset of 2.5 min at a fixed location. The reference rainfall R_{ref} is a Q2 rainfall mean computed within each PR pixel by considering the power density function of the PR beam. A standard error is computed alongside the mean reference rainfall value $\sigma_{\mathrm{footprint}}$, which represents the variability of the Q2 rainfall (at its native resolution) inside the PR footprint. This standard error is used to select the PR-Q2 reference pairs for which R_{ref} is considered trustworthy. The reference pixels are segregated into "robust" ($R_{\mathrm{ref}} > \sigma_{\mathrm{footprint}}$) and "nonrobust" ($R_{\mathrm{ref}} < \sigma_{\mathrm{footprint}}$) estimators. Nonrobust reference values are discarded for quantitative comparison. The PR rainfall statistical characteristics are preserved because the product remains free of undesirable impacts caused by resampling. A more detailed discussion concerning this point is provided in Kirstetter et al. (2012b). Figure 1c shows a zoom-in of the snapshot of TRMM PR shown in Fig. 1b. Figures 1d–g illustrates the processing steps performed on the Q2RadGC product. Figure 1d shows the original Q2RadGC product prior to processing, and Fig. 1e shows matching Q2RadGC after it has been resampled to the pixel resolution of TRMM PR. Data falling outside the swath of the TRMM overpass have been discarded. Figure 1f shows the Q2 product after the robustness condition has been applied. Figure 1g shows those pixels that were considered nonrobust and have therefore been discarded in subsequent analyses.

Next, matched data pairs are counted within 0.25° grid cells. This common grid was needed for composited data because the TRMM 2A25 product is specific for each overpass. If the number of matched pixels was less than 30 for a given 0.25° grid cell, then we deemed the sample size too small and do not consider those pairs for statistical evaluation hereafter. Figure 2a shows the distribution of total matched pairs between Q2 and PR for all overpasses combined in the 1-yr study. No considerations of the data quality, rainfall amounts, or sample sizes have been made in this plot; thus, it represents the theoretical maximum of data pairs for the study period. Figure 2b shows the distribution of nonzero PR-Q2 data pairs (i.e., both PR and Q2 rain rates are greater than 0 mm h^{-1}) following application of all processing steps including the robustness criterion to Q2 data, removal of pixels with HSRH values greater than 3200 m, and removal if the number of matched pairs is less than 30. The HSRH threshold was implemented in order to strike a balance between high-quality Q2 reference values, which are generally obtained at lower HSRH values, and sample sizes of matched pairs. The most pair-intensive areas are along the latitude of 35°, which corresponds to the location with the most frequent TRMM overpasses.

To compare TRMM PR's rainfall estimates using Q2 as a reference, we compute the bias, mean bias (MB), relative bias (RB), root-mean-squared error (RMSE), and Pearson linear correlation coefficient (CC). These statistics are defined as follows:

$$\mathrm{bias} = \left(\sum_{i=1}^{N} \mathrm{PR}_i - \sum_{i=1}^{N} \mathrm{Q2}_i \right), \tag{1}$$

$$\mathrm{MB} = \frac{1}{N} \left(\sum_{i=1}^{N} \mathrm{PR}_i - \sum_{i=1}^{N} \mathrm{Q2}_i \right), \tag{2}$$

$$\mathrm{RB} = \frac{\sum_{i=1}^{N} \mathrm{PR}_i - \sum_{i=1}^{N} \mathrm{Q2}_i}{\sum_{i=1}^{N} \mathrm{Q2}_i}, \tag{3}$$

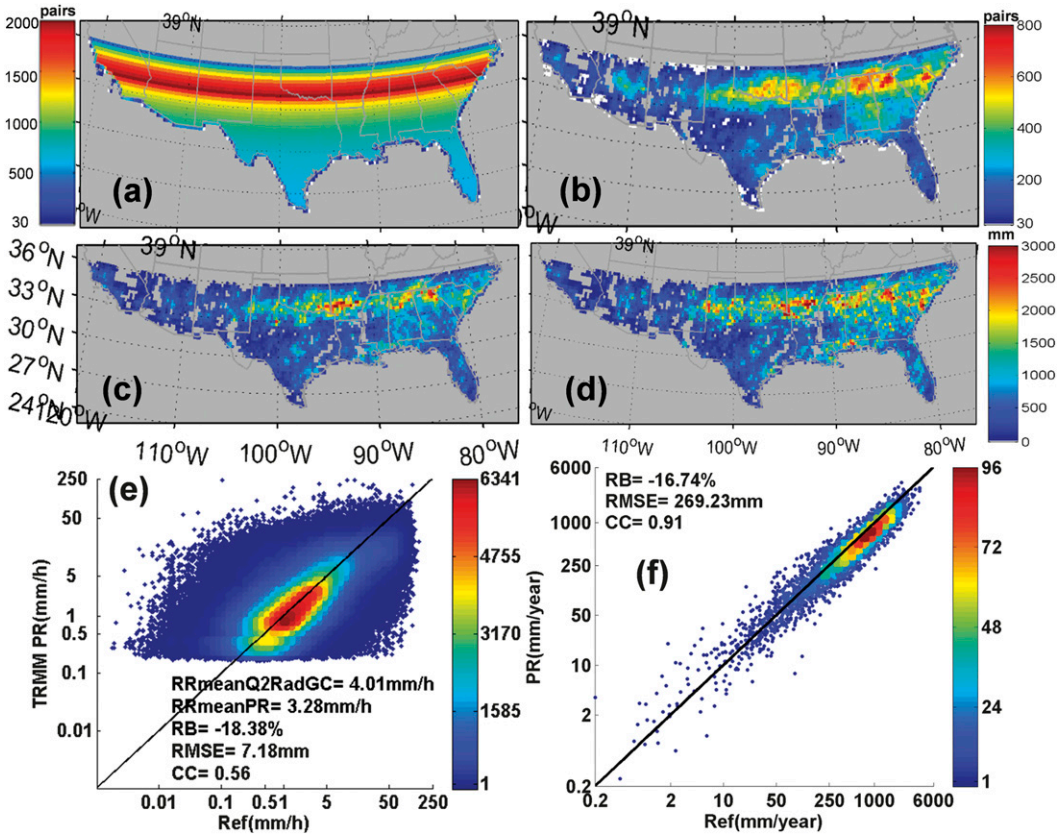

FIG. 2. (a) Theoretical maximum of PR-Q2 matched pairs for the study period. (b) Number of matched pairs with nonzero rainfall amounts following application of the robust criterion to the Q2RadGC product and removal of pixels with small sample sizes and HSRH > 3200 m. Total annual rainfall (mm) from (c) PR and (d) Q2RadGC. Density-colored scatterplots and statistics computed for (e) rainfall rates and (f) total annual rainfall accumulation.

$$\mathrm{RMSE} = \sqrt{\frac{1}{N}\sum_{i=1}^{N}(\mathrm{PR}_i - \mathrm{Q2}_i)^2}, \tag{4}$$

$$\mathrm{CC} = \frac{\mathrm{Cov}(\mathrm{PR}, \mathrm{Q2})}{\sigma_{\mathrm{Q2}}\sigma_{\mathrm{PR}}}, \tag{5}$$

where bias, MB, and RMSE are in units of mm h^{-1}; RB and CC are dimensionless; Cov refers to the covariance; and σ is the standard deviation. RB, when multiplied by 100, gives the degree of overestimation or underestimation in percentage. In Eqs. (1)–(5), N corresponds to the number of matched data pairs.

The contingency table statistics describing the probability of detection (POD), critical success index (CSI), and false alarm rate (FAR) are also used to evaluate PR performance. These indexes are computed based on the number of hits (H), false alarms (F), misses (M), and correct nulls (C) for data pairs exceeding a given rainfall threshold:

$$\mathrm{POD} = \frac{H}{H + M}, \tag{6}$$

$$\mathrm{CSI} = \frac{H}{H + F + M}, \tag{7}$$

$$\mathrm{FAR} = \frac{F}{H + F}. \tag{8}$$

3. Results and discussion

a. All grid cells combined

Figures 2c and 2d show the yearly accumulated rainfall distribution according to TRMM PR and ground radar–based Q2. The density-colored scatterplot in Fig. 2e shows that PR underestimates the average rain rate by 18.38% and is moderately correlated with Q2 with a CC of 0.56. If we consider the annual rainfall accumulation in Fig. 2f, we see that PR is highly correlated with Q2 as indicated by a CC of 0.91. This means that while PR and Q2 have only moderate agreement on the spatial distribution of instantaneous rainfall rates, they agree very well in capturing the annual spatial distributions of rainfall.

TABLE 1. Conditioned statistics for PR-Q2RadGC 5-min comparison.

Condition	Pairs	Mean (mm h^{-1}) Ref	Mean (mm h^{-1}) PR	CC	RMSE	MB (mm h^{-1})	RB (%)
1. Ref > 0 and PR > 0	1 142 724	3.68	3.23	0.55	6.91	−0.45	−12.29
2. Ref > 0 and PR > 0 and Robust ($R_{\mathrm{ref}} > \sigma_{\mathrm{footprint}}$)	959 332	3.96	3.27	0.56	7.13	−0.69	−17.58
3. Ref > 0 and PR > 0 and Robust ($R_{\mathrm{ref}} > \sigma_{\mathrm{footprint}}$) and HSRH filtration	906 539	4.01	3.27	0.56	7.18	−0.74	−18.38

The number of data samples for evaluation is affected by rainfall intermittency, the overpass frequency of TRMM PR, and censoring of reference values to improve its quality. Table 1 indicates there are a total of 1 142 724 PR-Q2 matched pairs for which the rain rates of both Q2 and PR are greater than 0 mm h^{-1}. After applying the robust criterion to Q2, the sample size drops to 959 332 samples, and the CC improves from 0.55 to 0.56. This criterion mainly filters out low reference values, as discussed in Kirstetter et al. (2012b), and thus increases the mean of the Q2 reference from 3.68 to 3.96 mm, having an impact on the bias. After pairs at relatively high HSRH values (>3200 m) have been filtered, we see the number of matched pairs decrease 5.5% to 906 539. The impact of the HSRH filter is shown to be insignificant on the overall statistics in Table 1.

Figure 3 shows POD, CSI, and FAR for different reference rainfall thresholds based on all valid matching pairs in which the rainfall estimated by PR and Q2 is greater than or equal to 0 mm h^{-1}. We note the general improvement of the POD and CSI from 0 to 0.5 mm h^{-1}, the latter value being close to the characteristic threshold

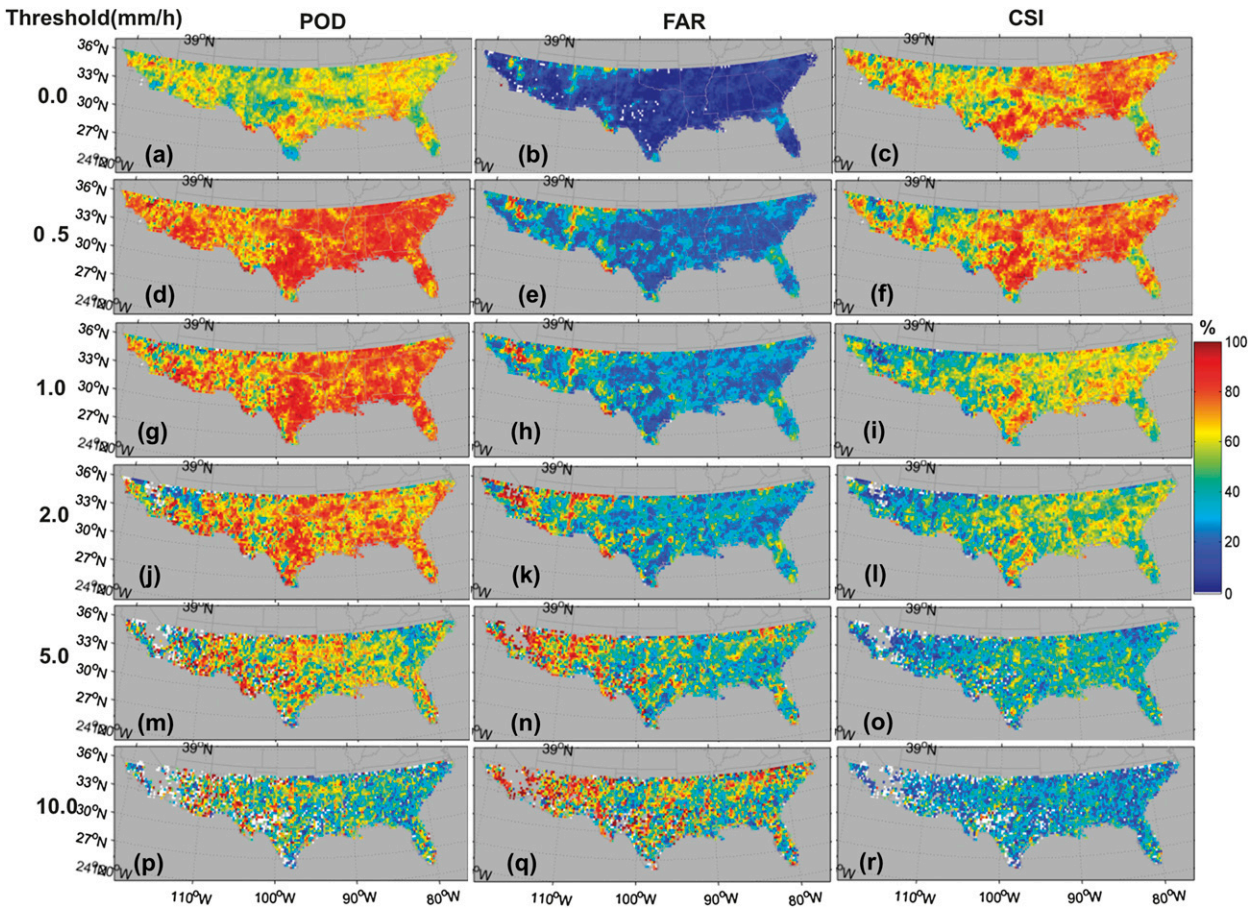

FIG. 3. Spatial distribution of unconditioned (left) POD, (middle) FAR, and (right) CSI based on different thresholds of (a)–(c) 0, (d)–(f) 0.5, (g)–(i) 1, (j)–(l) 2, (m)–(o) 5, and (p)–(r) 10 mm h^{-1}.

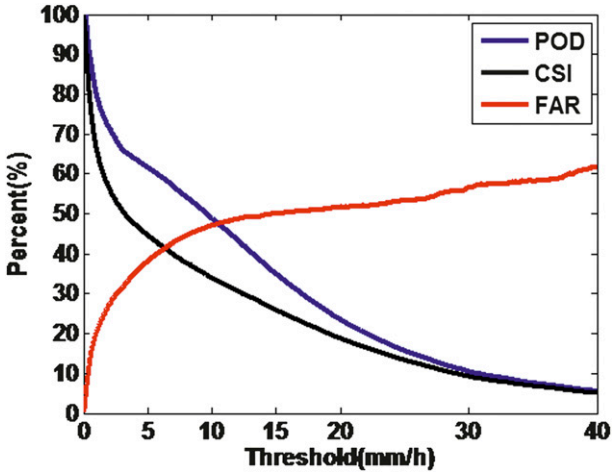

FIG. 4. Contingency table statistics for PR as a function of reference rainfall rates shown on the abscissa. Only pairs of positive PR and reference rainfall values are used.

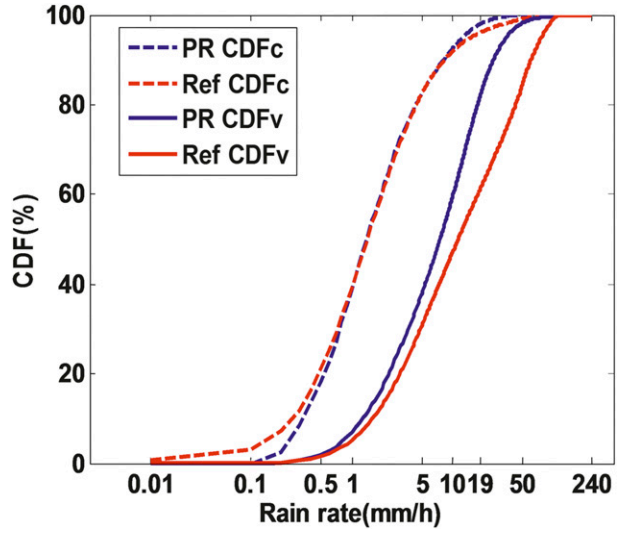

FIG. 5. CDFc and CDFv for PR and Q2 references.

defining the detection capabilities of the PR. This improvement illustrates again that the PR misses the lightest intensities, with large differences between the Great Plains and mountainous areas. Above 0.5 mm h^{-1}, higher FAR values and noisy POD patterns are consistently pronounced in the mountainous regions of the west, probably to be linked to poor performance of the surface reference technique (SRT). Figure 4 shows POD, CSI, and FAR as a function of reference rainfall thresholds based on the robust dataset with HSRH filtering. Because only positive rainfall pairs are considered, POD and CSI are high when the threshold is set to very light amounts (e.g., 0.1 mm h^{-1}). The POD and CSI decrease dramatically and the FAR increases consistently when considering higher thresholds. At thresholds greater than 12 mm h^{-1}, POD and CSI decrease dramatically and FAR asymptotically approaches 61.71%. This indicates that PR has deficiency in detecting higher rain rates, probably because of insufficient attenuation correction of the PR radar signal as suggested by Amitai et al. (2009) and Kirstetter et al. (2012b).

Cumulative distributions of rain rates of PR and Q2 rainfall in terms of occurrence (CDFc) and volume (CDFv) are used to characterize the PR's ability to detect different rainfall intensities. Figure 5 shows that PR poorly detects the lightest rain rates (<0.1 mm h^{-1}) but presents similar CDFc with the Q2 reference for rain rates greater than 1 mm h^{-1}. The CDFv indicates that for PR, rain rates in the range of 0.3–25 mm h^{-1} contribute nearly entirely to the total rainfall volume while the contribution from higher rain rates (>25 mm h^{-1}) is significant for the reference. As an example, PR has a limited cumulated occurrence (7%) of rain rates greater than 10 mm h^{-1} for a cumulated contribution up to 40%. Q2, on the other hand, has a similar total rainfall contribution of 40% when the rain rates are greater than 20 mm h^{-1}. This indicates that PR underestimates higher rainfall rates (>20 mm h^{-1}), probably because of insufficient correction of signal attenuation losses as suggested by Wolff and Fisher (2008) for the 2A25, version 6, and still significant of version 7 (Kirstetter et al. 2012b). There are several factors that could explain the PR overestimation for moderate rain rates of 5–20 mm h^{-1} including incorrect rainfall classification, overcorrection of the attenuated radar signal, incorrect *Z–R* relationship, and geometric effects (i.e., parallax issue outside of nadir).

b. *Spatial analysis*

TRMM PR classifies rainfall as convective, stratiform, and others (Iguchi et al. 2000). Figure 6 shows the spatial distribution of convective and stratiform occurrences as well as the scatterplots of convective and stratiform rain types derived independently from PR and Q2. We can see that the patterns of convective and stratiform echoes according to PR and Q2 are quite similar. Both sensors detect lower occurrence (<25%) of convective rain events over most areas, with locally higher convective occurrence (25%–50%) in the mountainous areas and central Florida. However, as shown in Fig. 6e, PR detects more convective rain types than Q2 over the Great Plains (especially in Texas, Alabama, and Florida) and less over the western mountainous part of the CONUS. The scatterplots in Figs. 6g and 6h indicate that the spatial distributions of both convective and stratiform echoes from PR are poorly correlated with those of Q2 with a CC of 0.33. The biggest difference, however, is the propensity for PR to detect more convective echoes than

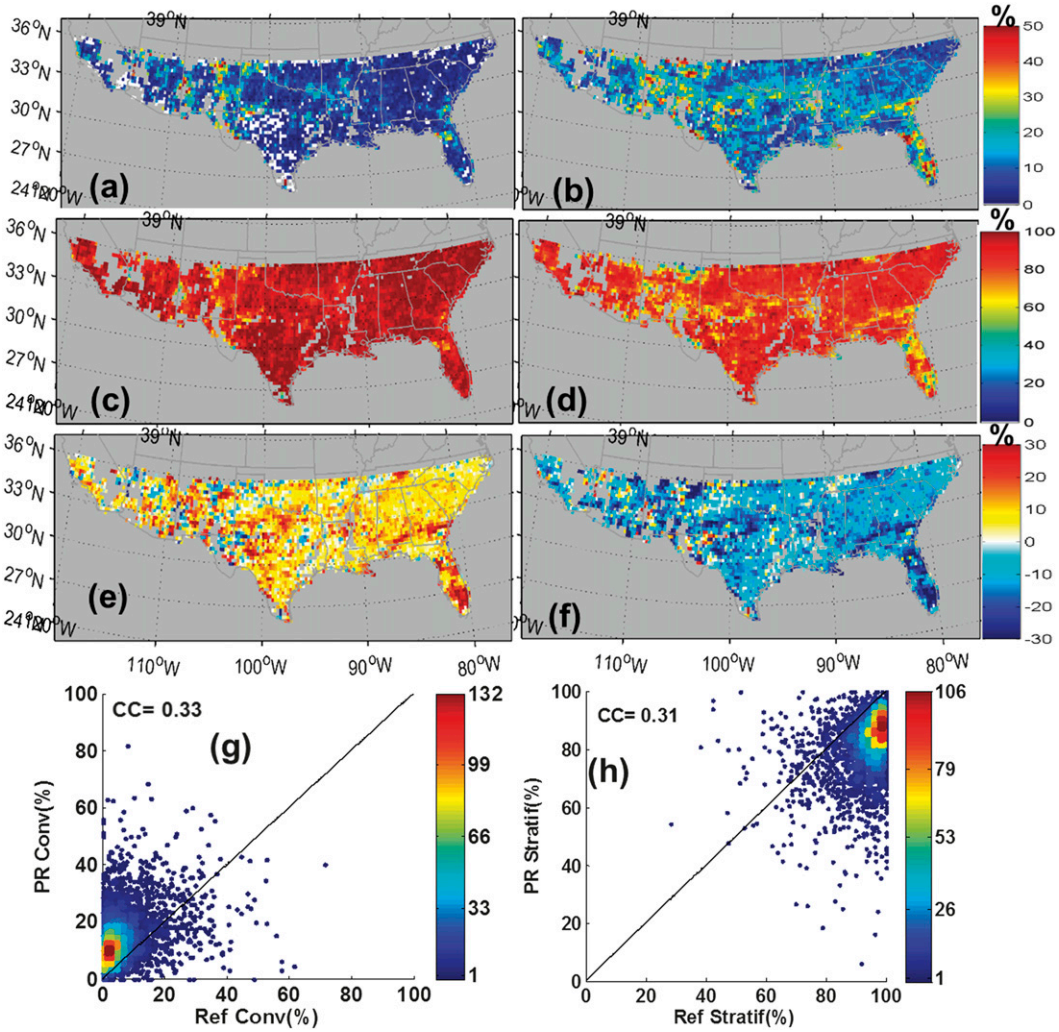

FIG. 6. Convective rain type occurrence distribution for (a) Q2 reference and (b) PR, stratiform rain type occurrence distribution for (c) Q2 reference and (d) PR, (e) the difference of (b) and (a),(f) the difference of (d) and (c),(g) scatterplot of (a) and (b), and (h) scatterplot of (c) and (d).

Q2. While there is no evidence that the Q2 classification may be more accurate than the PR, this particular characteristic will be revisited in the spatial rainfall error quantification, as it can potentially explain bias in rainfall rate estimation due to more classification of convective rain types from the PR relative to the reference.

Convective events usually bring localized, intense rainfall in a short amount of time while stratiform events are associated with weaker rainfall but lasting for a relatively long time period over larger areas. Insights into convective and stratiform contributions in rain events go beyond evaluating PR QPEs in that they will benefit users of the data interested in hydrologic extremes such as floods and landslides. Figure 7 shows the spatial distributions of total convective and stratiform rainfall, percent contribution from convective and stratiform echoes to total rainfall, and scatterplots between PR and Q2. Figures 6a–c indicate that the patterns of PR and Q2 convective rainfall accumulation are similar, but PR underestimates the convective accumulation relative to Q2. Figure 7c indicates that the patterns are correlated (CC = 0.63) and PR underestimates the convective accumulation by 48.82%. Accordingly, Figs. 7d–f indicate that Q2 presents more stratiform rainfall accumulation than PR, especially over Texas and Alabama, Tennessee, North Carolina, and South Carolina. Figure 7f demonstrates that the stratiform rainfall pattern of PR is more correlated with Q2 (CC = 0.86) than for the convective rainfall, and PR underestimates the stratiform rainfall accumulation by 5.13%.

Considering the percent contribution from the two rain types, we can see from Figs. 7g, 7h, 7j, and 7k that

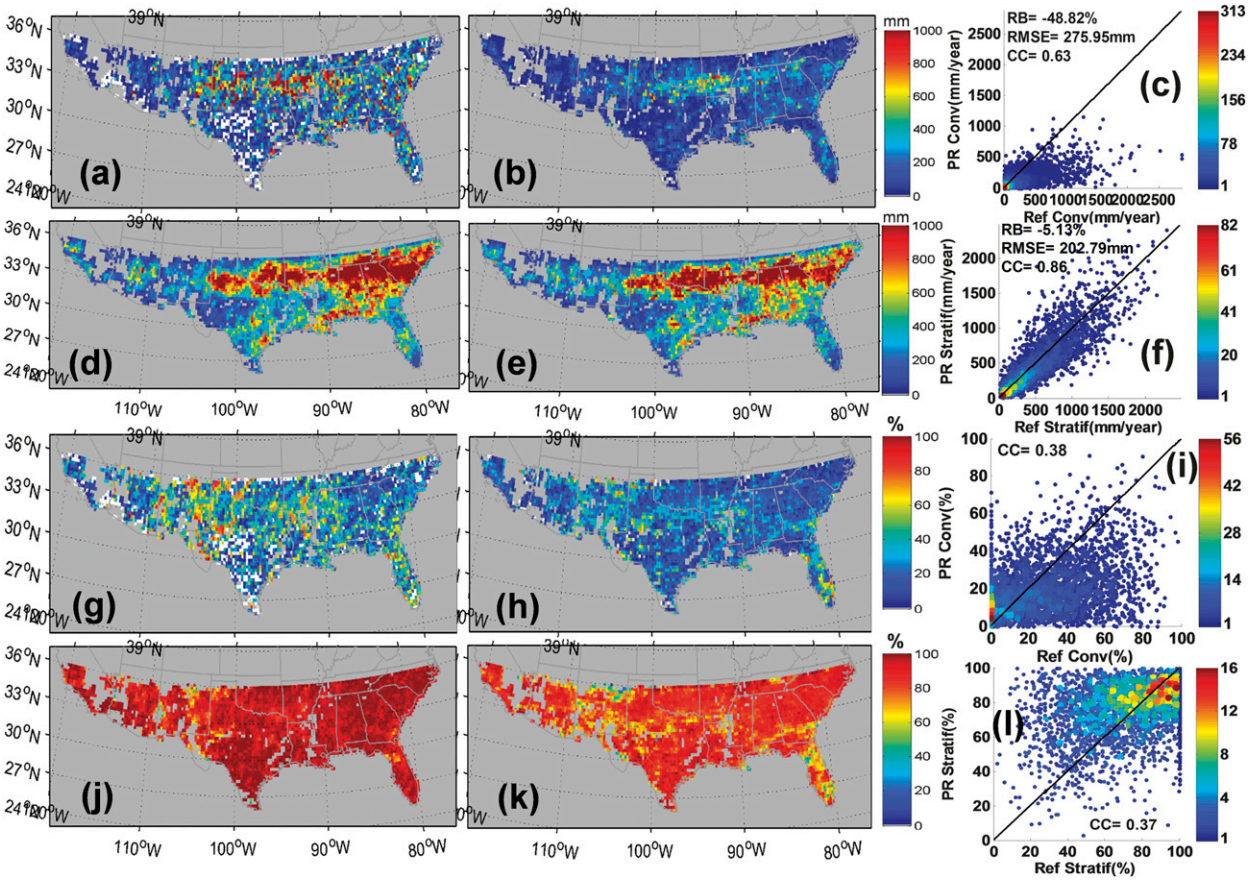

FIG. 7. Total convective rainfall from the (a) Q2 reference, (b) PR, and (c) scatterplot between the two; (d)–(f) as in (a)–(c), but for stratiform rainfall. The percentage of contribution from convective echoes for (g) Q2 reference, (h) PR, and (i) scatterplot between the two; (j)–(l) as in (g)–(i), but for stratiform echoes.

the spatial patterns of PR types are similar to Q2. The scatterplots in Figs. 7i and 7l indicate that both convective and stratiform distribution patterns of PR are poorly correlated with Q2 with a CC of approximately 0.38 and 0.37, respectively. However, PR overestimates the convective contribution relative to Q2.

Figure 8 shows the spatial distributions of POD, CSI, and FAR with a threshold set to 1 mm h^{-1} for the first column to focus on moderate rainfall and with a threshold set to 10 mm h^{-1} for the second column to focus on high rainfall rates. With the threshold set at 1 mm h^{-1}, PR generally shows good POD (59.84% of areas have POD above 80%), good CSI (34.48% of areas have CSI above 50%) and low FAR (only 3.21% of areas have FAR above 50%). Plains and mountainous areas are distinct, with lower detectability of PR noted in New Mexico, Arizona, and California. We note consistently higher FAR values in the mountainous regions of the west. A potential explanation is that the higher false alarms over mountainous regions may be caused by poor performance of the SRT. It is unlikely that these regions are poorly sampled by Q2, which also suffers by beam blockages, because we restricted the Q2 reference dataset to areas of good radar sampling with HRSH $<$ 3200 m. Two other spots of high FAR values are noticeable in Texas. Figure 5f shows that these spots correspond to a significant overestimation (>15%) of the PR convective rainfall classification relative to the reference. In this case one could relate this PR overestimation of surface rain rate to a misclassification of rainfall type. We discuss this point further in section 3c below.

With the threshold set to 10 mm h^{-1}, scores are generally worse with lower POD (9.32% of areas have POD above 80%), lower CSI values (only 2.52% of areas have CSI above 80%), and higher FAR (11.02% of areas have FAR above 80%). The POD tends to increase toward the west, but this is offset with an increase in the FAR over the mountainous areas. The spatial correlation between areas with FAR values above 0.6 in Fig. 8f and the rainfall convective misclassification of PR relative to the reference in Fig. 6 are now becoming more evident.

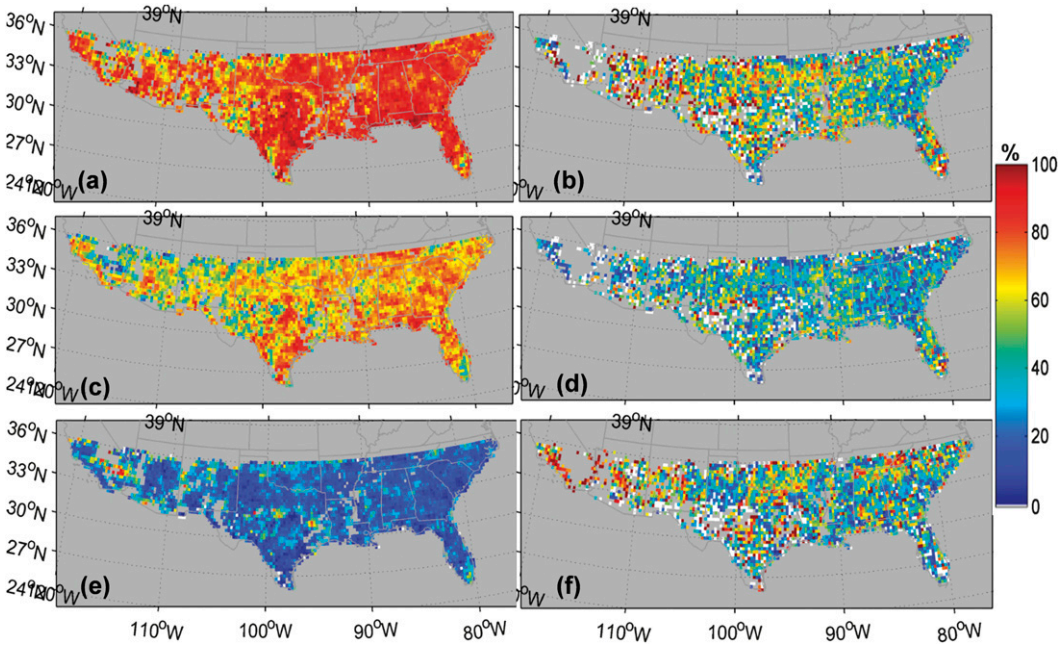

FIG. 8. Spatial distribution of (top) POD, (middle) CSI, and (bottom) FAR for rainfall thresholds of (a),(c),(e) 1 mm h^{-1} and (b),(d),(f) 10 mm h^{-1}.

Figure 9 reveals the spatial distribution maps of bias, RB, RMSE, and CC and the occurrences PDFc and CDFc of the error statistics. Figures 9a, 9b, and 9e indicate that PR underestimates rainfall amounts for approximately 75% of the total area. Figure 8f shows that the rainfall was underestimated by about 20%–40% over 32% of the total study area. The most significant overestimates by PR according to RB (Fig. 9b) occur in the western mountainous regions, which can be explained by failures in the SRT algorithm associated with complex terrain. The other overestimation areas are in north Texas and Alabama and are correlated with the convective misclassification of PR relative to the reference. Regarding RMSE, Fig. 9h shows that 37% of the total area has RMSE ranging from 3 to 6 mm, and 14% of the total area has RMSE > 10 mm. The RMSE spatial pattern (Fig. 9c) is correlated with the intensity of the rainfall amounts (Figs. 2c,f), with lower RMSE values (2 and 4 mm) over mountainous regions and higher values (>7mm) over the Great Plains. The correlation between PR and the reference is moderate (CC values lower than 0.7 over 68% of the total area). The correlation is notably degraded over mountainous regions (CC < 0.4) probably because of issues with the SRT.

c. Discussion

The following factors (and combinations therein) potentially explain why PR more frequently estimates moderate rain rates from 5 to 20 mm h^{-1} (Fig. 5b): incorrect rainfall classification, overcorrection of the attenuated radar signal, poor performance of the SRT, ground clutter in mountainous regions, incorrect *Z–R* relationship, and geometric effects (i.e., parallax issue outside of nadir). As shown in Fig. 4, FAR increases correspondingly as the rain rate threshold increases, indicating that PR overdetects high rain rates relative to the time and location of the Q2 reference. Regions with significant FAR (Fig. 8) and overestimation of rainfall rates (Fig. 9) are correlated with PR misclassification of rainfall type relative to the reference (see Figs. 6, 7). Iguchi et al. (2009) mentioned the model for vertical profile of specific attenuation used in the 2A25, version 6, algorithm is particularly strong (i.e., specific attenuation is 0.3–0.4 dB km^{-1} greater in version 7 compared to version 6 for convection above the freezing level); thus, misclassifications of stratiform echoes to convective will likely result in such overestimation of moderate rain rates. While there is no evidence we should expect the same in version 7, this could be considered for explaining such biases of the PR relative to the reference.

A clear error separation can be made between mountains and the Great Plains. It is likely the SRT method is triggered over complex terrain, resulting in high-amplitude biases. Over the Great Plains, dominant error factors are more probably related to the rainfall classification, attenuation correction, and *Z–R* relationship. Generally, the 2A25 algorithm detects more convection than Q2. The greatest amounts of convective

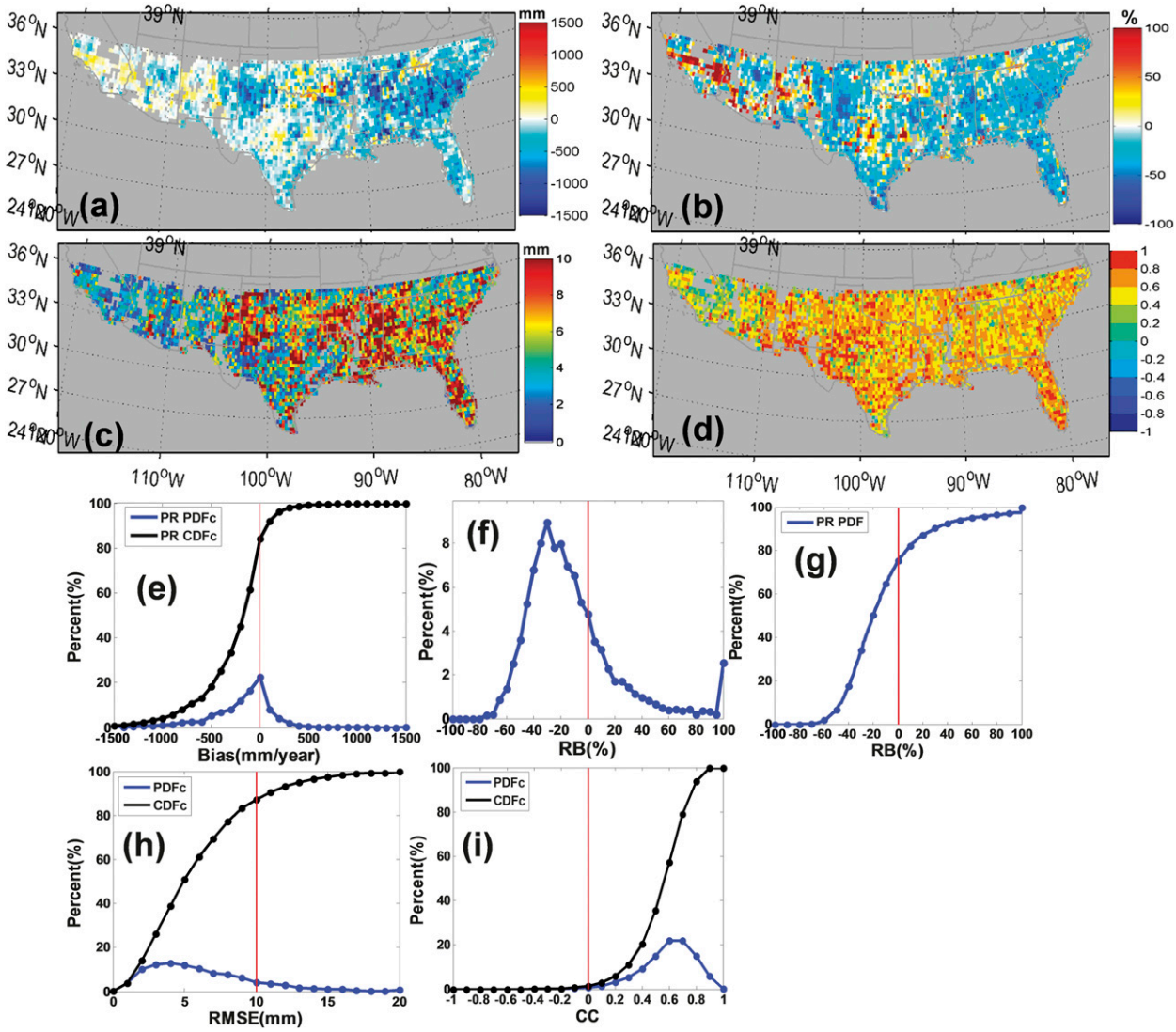

FIG. 9. Spatial distribution of (a) bias (mm), (b) RB (%), (c) RMSE (mm), and (d) CC. (e) PDFc and CDFc for the bias, (f) PDFc for RB, (g) CDFc for RB, (h) PDFc and CDFc for RMSE, and (i) PDFc and CDFc for CC.

overestimation occur over the southern part (Texas, Louisiana, Mississippi, Alabama, Georgia, and Florida), which corresponds to the regions where intense precipitation ($>10\,\mathrm{mm\,h^{-1}}$) occurs most frequently (Lin and Hou 2012). However, these patterns do not correspond to the spatial variations of biases of PR relative to Q2. The PR convective (stratiform) rainfall contribution is generally lower (greater) than Q2 (Figs. 7a,b), which implies issues in the attenuation correction of the PR signal, NUBF, and/or *Z–R* relationship.

4. Summary and conclusions

This study provides a spatially distributed evaluation of TRMM PR-based precipitation rates and types over the southern CONUS using NOAA/NSSL's ground radar-based national mosaic QPE product (Q2) from December 2009 to November 2010 in anticipation of NASA's future GPM mission. Given their resolutions, NMQ products are well suited for evaluating rainfall estimates from spaceborne sensors like the PR aboard the low-Earth-orbiting TRMM satellite. Both products were resampled onto a common grid at a 0.25° resolution, and a conservative approach was followed to ensure a robust comparison. Annual total precipitation, point-to-point-based scatterplots, comparison of precipitation-type products, bias, RB, RMSE, CC, POD, CSI, and FAR were all applied to evaluate the TRMM PR–based products. The main findings are summarized as follows.

1) PR captures the spatial pattern of total annual rainfall with a CC of 0.91.
2) PR detects more convection than Q2.
3) TRMM PR and Q2 have very similar spatial patterns of total convective and stratiform rainfall types, with a CC of 0.63 for convective and 0.86 for stratiform echoes.
4) Despite these strong correlations of precipitation type, PR's total annual precipitation from convection is 48.82% less than that by Q2, and its contribution to total annual precipitation from stratiform echoes is 5.13% less than from the Q2 reference.
5) In terms of instantaneous rain rates in a year, PR is moderately correlated with Q2 with a mean CC of 0.56 (Fig. 2e).
6) Regarding regional error characteristics, TRMM PR overestimates in western mountainous areas, presumably because of failure of the surface reference technique used in the PR algorithm.
7) TRMM PR underestimates precipitation magnitude by a great margin in the southeastern CONUS, which may be related to specific microphysics not well described in the 2A25 algorithm. Further research is needed to explore the impacts of the assumptions used in the algorithms relative to observed participate drop size distributions.
8) TRMM PR has high RMSE (>6 mm) in eastern parts of New Mexico, northwest Texas, south Arkansas, south Tennessee, north Alabama, north Georgia, and south Florida.
9) PR has high POD (>80%), moderate CSI (>60%) and low FAR in the eastern flat areas of the CONUS when the rain rate threshold is set to $1\,\mathrm{mm\,h^{-1}}$, but these statistics degrade significantly when the threshold is increased to $10\,\mathrm{mm\,h^{-1}}$.

A quantification of the uncertainty of these rainfall estimates will be quite useful to users of the data, including hydrologists, which is the principal aim of this study. Given that the TRMM PR has more than 10 years of product generation since its launch in 1997 and the NMQ is under retrospective production going back to 2002, future work will be potentially carried out to explore the climatological spatial patterns of rain rates and rain types (i.e., convective and stratiform) derived by TRMM PR against NMQ at multiseasonal, interannual, and decadal time scales. This will give us further understanding of TRMM PR's spatially distributed performance. Moreover, future investigations with anticipation of the GPM launch in 2014 will likely advance our understanding of the spatial features of spaceborne radar precipitation products extended from the TRMM-covered CONUS to the whole CONUS and beyond. This study develops a benchmark to be used for the GPM-DPR era. With dual-frequency radar, we expect the rainfall estimates will have reduced RMSE and systematic biases compared to the ground reference. We will be able then to establish the areas with greatest (lowest) improvements and will be able to relate these trends to error factors.

Acknowledgments. The authors wish to acknowledge the OU and NOAA/NSSL team for providing the NMQ/Q2 products. This work was funded by a postdoctoral grant from the NASA Global Precipitation Measurement Mission Ground Validation Program and was also supported by the Multi-function Phased-Array Radar (MPAR) Project at the University of Oklahoma Advanced Radar Research Center. Partial funding was provided by the NOAA/Office of Oceanic and Atmospheric Research under NOAA–University of Oklahoma Cooperative Agreement NA17RJ1227.

REFERENCES

Abdella, Y., and K. Alfredsen, 2010: Long-term evaluation of gauge-adjusted precipitation estimates from a radar in Norway. *Hydrol. Res.,* **41,** 171–192, doi:10.2166/nh.2010.011.

Adeyewa, Z. D., and K. Nakamura, 2003: Validation of TRMM radar rainfall data over major climatic regions in Africa. *J. Appl. Meteor.,* **42,** 331–347, doi:10.1175/1520-0450(2003)042<0331:VOTRRD>2.0.CO;2.

Amitai, E., X. Llort, and D. Sempere-Torres, 2009: Comparison of TRMM radar rainfall estimates with NOAA next-generation QPE. *J. Meteor. Soc. Japan,* **87A,** 109–118, doi:10.2151/jmsj.87A.109.

——, W. Petersen, X. Llort, and S. Vasiloff, 2012: Multiplatform comparisons of rain intensity for extreme precipitation events. *IEEE Trans. Geosci. Remote Sens.,* **50,** 675–686, doi:10.1109/TGRS.2011.2162737.

Benjamin, S. G., and Coauthors, 2004: An hourly assimilation-forecast cycle: The RUC. *Mon. Wea. Rev.,* **132,** 495–518, doi:10.1175/1520-0493(2004)132<0495:AHACTR>2.0.CO;2.

Berges, J., I. Jobard, F. Chopin, and R. Roca, 2010: EPSAT-SG: A satellite method for precipitation estimation; Its concepts and implementation for the AMMA experiment. *Ann. Geophys.,* **28,** 289–308, doi:10.5194/angeo-28-289-2010.

Ebert, E., 2007: Methods for verifying satellite precipitation estimates. *Measuring Precipitation from Space,* V. Levizzani, P. Bauer, and F. J. Turk, Eds., Springer, 345–356.

Grimes, D. I. F., and M. Diop, 2003: Satellite-based rainfall estimation for river flow forecasting in Africa. I: Rainfall estimates and hydrological forecasts. *Hydrol. Sci. J.,* **48,** 567–584, doi:10.1623/hysj.48.4.567.51410.

Hong, Y., and R. F. Adler, 2007: Towards an early-warning system for global landslides triggered by rainfall and earthquake. *Int. J. Remote Sens.,* **28,** 3713–3719, doi:10.1080/01431160701311242.

——, ——, and G. Huffman, 2007: An experimental global prediction system for rainfall-triggered landslides using satellite remote sensing and geospatial datasets. *IEEE Trans. Geosci. Remote Sens.,* **45,** 1671–1680, doi:10.1109/TGRS.2006.888436.

Huffman, G. J., and Coauthors, 2007: The TRMM multisatellite precipitation analysis (TMPA): Quasi-global, multiyear,

combined-sensor precipitation estimates at fine scales. *J. Hydrometeor.,* **8,** 38–55, doi:10.1175/JHM560.1.

Iguchi, T., R. Meneghini, J. Awaka, T. Kozu, and K. Okamoto, 2000: Rain profiling algorithm for TRMM precipitation radar data. *Adv. Space Res.,* **25,** 973–976, doi:10.1016/S0273-1177(99)00933-3.

——, T. Kozu, J. Kwiatkowski, R. Meneghini, J. Awaka, and K. Okamoto, 2009: Uncertainties in the rain profiling algorithm for the TRMM precipitation radar. *J. Meteor. Soc. Japan,* **87A,** 1–30, doi:10.2151/jmsj.87A.1.

Kirstetter, P.-E., Y. Hong, J. Gourley, M. Schwaller, W. Petersen, and J. Zhang, 2012a: Comparison of TRMM 2A25 products, version 6 and version 7, with NOAA/NSSL ground radar–based National Mosaic QPE. *J. Hydrometeor.,* **14,** 661–669, doi:10.1175/JHM-D-12-030.1.

——, and Coauthors, 2012b: Toward a framework for systematic error modeling of spaceborne precipitation radar with NOAA/NSSL ground radar-based National Mosaic QPE. *J. Hydrometeor.,* **13,** 1285–1300, doi:10.1175/JHM-D-11-0139.1.

Kozu, T., and Coauthors, 2001: Development of precipitation radar onboard the Tropical Rainfall Measuring Mission (TRMM) satellite. *IEEE Trans. Geosci. Remote Sens.,* **39,** 102–116, doi:10.1109/36.898669.

Kummerow, C., W. Barnes, T. Kozu, J. Shiue, and J. Simpson, 1998: The tropical rainfall measuring mission (TRMM) sensor package. *J. Atmos. Oceanic Technol.,* **15,** 809–817, doi:10.1175/1520-0426(1998)015<0809:TTRMMT>2.0.CO;2.

Lebel, T., and Coauthors, 2009: AMMA-CATCH studies in the Sahelian region of West-Africa: An overview. *J. Hydrol.,* **375,** 3–13, doi:10.1016/j.jhydrol.2009.03.020.

Li, L., C. S. Ngongondo, C.-Y. Xu, and L. Gong, 2013: Comparison of the global TRMM and WFD precipitation datasets in driving a large-scale hydrological model in southern Africa. *Hydrol. Res.,* doi:10.2166/nh.2012.175, in press.

Li, X.-H., Q. Zhang, and C.-Y. Xu, 2012: Suitability of the TRMM satellite rainfalls in driving a distributed hydrological model for water balance computations in Xinjiang catchment, Poyang lake basin. *J. Hydrol.,* **426–427,** 28–38, doi:10.1016/j.jhydrol.2012.01.013.

Lin, X., and A. Y. Hou, 2012: Estimation of rain intensity spectra over the continental United States using ground radar-gauge measurements. *J. Climate,* **25,** 1901–1915, doi:10.1175/JCLI-D-11-00151.1.

Maddox, R. A., J. Zhang, J. J. Gourley, and K. W. Howard, 2002: Weather radar coverage over the contiguous United States. *Wea. Forecasting,* **17,** 927–934.

Parkes, B., F. Wetterhall, F. Pappenberger, Y. He, B. Malamud, and H. Cloke, 2013: Assessment of a 1-hour gridded precipitation dataset to drive a hydrological model: A case study of the summer 2007 floods in the Upper Severn, UK. *Hydrol. Res.,* **44,** 89–105, doi:10.2166/nh.2011.025.

Stephens, G. L., and C. D. Kummerow, 2007: The remote sensing of clouds and precipitation from space: A review. *J. Atmos. Sci.,* **64,** 3742–3765, doi:10.1175/2006JAS2375.1.

Vasiloff, S. V., and Coauthors, 2007: Improving QPE and very short term QPF. *Bull. Amer. Meteor. Soc.,* **88,** 1899–1911, doi:10.1175/BAMS-88-12-1899.

Wolff, D. B., and B. L. Fisher, 2008: Comparisons of instantaneous TRMM ground validation and satellite rain-rate estimates at different spatial scales. *J. Appl. Meteor. Climatol.,* **47,** 2215–2237.

——, and ——, 2009: Assessing the relative performance of microwave-based satellite rain-rate retrievals using TRMM ground validation data. *J. Appl. Meteor. Climatol.,* **48,** 1069–1099, doi:10.1175/2008JAMC2127.1.

——, D. A. Marks, E. Amitai, D. S. Silberstein, B. L. Fisher, A. Tokay, J. Wang, and J. L. Pippitt, 2005: Ground validation for the Tropical Rainfall Measuring Mission (TRMM). *J. Atmos. Oceanic Technol.,* **22,** 365–380, doi:10.1175/JTECH1700.1.

Yang, S., W. S. Olson, J. J. Wang, T. L. Bell, E. A. Smith, and C. D. Kummerow, 2006: Precipitation and latent heating distributions from satellite passive microwave radiometry. Part II: Evaluation of estimates using independent data. *J. Appl. Meteor. Climatol.,* **45,** 721–739, doi:10.1175/JAM2370.1.

Zeweldi, D. A., and M. Gebremichael, 2009: Sub-daily scale validation of satellite-based high-resolution rainfall products. *Atmos. Res.,* **92,** 427–433, doi:10.1016/j.atmosres.2009.01.001.

Zhang, J., and Coauthors, 2011: National Mosaic and Multi-Sensor QPE (NMQ) system: Description, results, and future plans. *Bull. Amer. Meteor. Soc.,* **92,** 1321–1338, doi:10.1175/2011BAMS-D-11-00047.1.